nature geoscience

SUPPLEMENTARY INFORMATION

DOI: 10.1038/NGEO2094

Solar forcing of North Atlantic surface temperature and salinity over the past millennium

Paola Moffa-Sánchez, Andreas Born, Ian R. Hall, David J.R. Thornalley, Stephen Barker

1- Supplementary methods

- **Paired $\delta^{18}O$ and Mg/Ca measurements**

Between 6-20 *Globorotalia inflata* tests were picked from the 300-355 µm size fraction for paired $\delta^{18}O$ and Mg/Ca measurements. The specimens were crushed and cleaned following the protocol outlined by ref. 1. The samples were analysed using a Thermo Scientific Element XR Inductive Coupled Plasma Mass Spectrometry at Cardiff University with an analytical precision for Mg/Ca ratios of better than 2.5%. Calculation of mean shell weights and investigation of the co-variability of Mg/Ca record to metals such as Fe, Mn and Al shows that no secondary effects, such as partial dissolution or trace metal contamination, have altered the primary temperature signal in the Mg/Ca record. Mg/Ca values were converted to calcification temperatures using $Mg/Ca = 0.675 \exp(0.1xT)$ after the core-top calibration by ref. 2. The use of this calibration is appropriate as both studies (i) used the small morphotypes of *G. inflata*, (ii) avoided encrusted shells (iii) picked same size fraction and (iv) the core locations are situated in close geographic proximity.

Stable oxygen isotope measurements were carried out on a Thermo Finnigan MAT 252 isotope ratio mass spectrometer coupled to a Kiel II carbonate preparation device at Cardiff University. The isotopic results are reported as a per mil deviation from the Vienna Pee Dee Belemnite scale (‰ VPDB) with an external reproducibility of carbonate standards (NBS19) was better than 0.08 ‰ for $\delta^{18}O$.

$\delta^{18}O_{sw}$ calculations were estimated using the temperature equation from ref. 3 and the salinity estimates were calculated after the North Atlantic Ocean $\delta^{18}O_{sw}$ – Salinity relationship from ref [4] of: $Salinity = (\delta^{18}O_{sw} - 32.45)/ 0.94)$.

The mean error in the temperature estimates is ±1.14°C including analytical (±3%) and calibration error (±1.1°C)[5]. The $\delta^{18}O_c$ measurement error of ±0.08‰ and the temperature error effects on the $\delta^{18}O_{sw}$ calculation result in a $\delta^{18}O_{sw}$ error of ±0.29‰. Based on calculations of the uncertainties in the relationship between $\delta^{18}O_{sw}$ and salinity from ref. 5, a salinity error of ±0.8 is used.

- **Core-chronology for RAPiD-17-5P**

Twelve ^{14}C AMS dates were measured from monospecific samples of *Globigerina bulloides* (>250μm) (Table S1, Figure S1). A mass of approximately 12 mg per sample was picked (equivalent to ~1000 individuals). Measurements were made at the NERC-Radiocarbon Laboratory, East Kilbride, U.K. The radiocarbon ages were converted to calendar years using Marine09[6] in CALIB 6.3[7]. The mean global reservoir correction of 405 years is justified as the core site lies in the pathway of the North Atlantic Current which is of tropical origin. Additionally, this reservoir correction has been used in several Holocene sediment cores from the Iceland Basin (e.g. ref. 2,8). We have also accounted for uncertainties in local reservoir correction (ΔR) of 50 years.

Code	Depth (cm)	Radiocarbon Age ±1σ (Yrs BP)	$\delta^{13}C$ (‰ VPDB)	95% confidence Age intervals (Yrs AD)		Calibrated Age (Yrs AD)
				Upper Limit	Lower Limit	
SUERC-15709	0.5	591±35	-0.4	1896	1572	1727
SUERC-46869	16.5	744±37	0.8	1673	1464	1565
SUERC-35766	34.5	874±35	-0.3	1588	1346	1456
SUERC-46870	47	1156±37	-0.3	1341	1094	1241
SUERC-35769	67.25	1416±37	-0.6	1134	829	982
SUERC-46871	78.5	1543±37	-0.3	996	712	850
SUERC-15710	96.5	1738±37	-0.3	782	529	660
SUERC-46872	125	2206±37	-0.6	311	-6	146
SUERC-46876	149	2406±37	-0.6	64	-289	-91
SUERC-15713	200.5	2852±37	-0.5	-444	-785	-653
SUERC-46877	248	3258±37	-0.6	-1011	-1260	-1138
SUERC-14101	750	8823±35	-1.3	-7472	-7590	-7535

Table S1. Radiocarbon ages from RAPiD-17-5P.

The core-chronology was constructed using a linear fit through the twelve radiocarbon dates obtained for the top 750 cm, which results in a sedimentation rate of approximately 100 cm/kyr for the last 9000 years (y=1808.9-12.416x; R^2=0.999) (Figure S1). We suggest that the goodness of fit demonstrates the probable lack of abrupt changes in the rate of the sediment deposition during the time interval studied (note: the linear fit through the dates for the top 250 cm is very similar (y = 1780.8-12.069x) to that of the top 750 cm with an R^2 value of 0.995. The core was sampled at 0.5 cm intervals and thus each data point represents an integrated time of 6.21 years. The core-top of RAPiD-17-5P was lost as the piston core over penetrated[9].

The statistical package; BChron[10,11] was used to calculate the 95% uncertainty on the calibrated ages (Table S1) and the 95% probability envelope for the time period studied using a Bayesian approach (Figure S2).

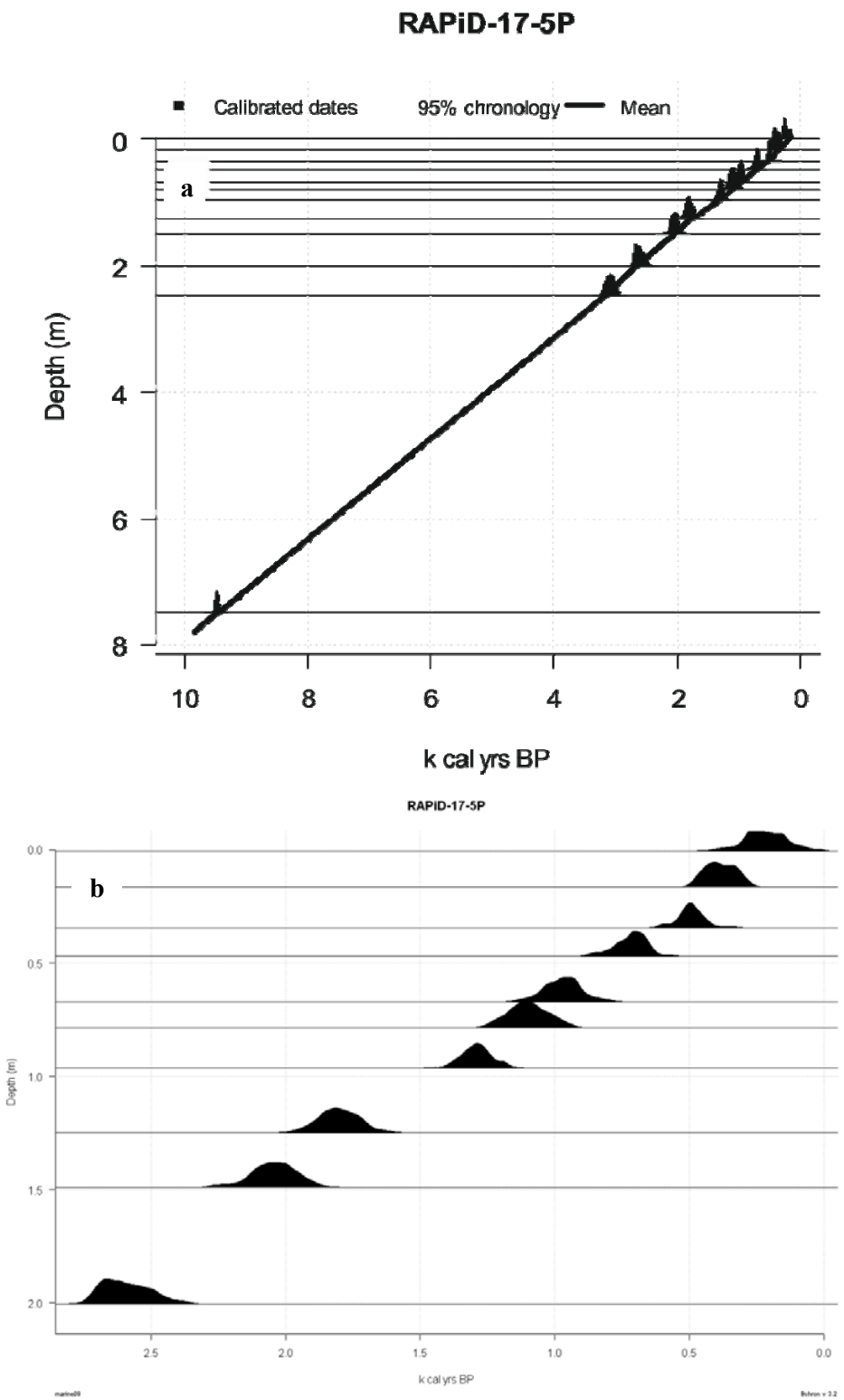

Figure S1. RAPiD-17-5P radiocarbon calibrated ages against depth of the top 750cm (a) and top 250cm (b), respectively. Each date is represented by the probability distribution of the intersection between the radiocarbon ages at those depths and the Marine09 calibration curve.

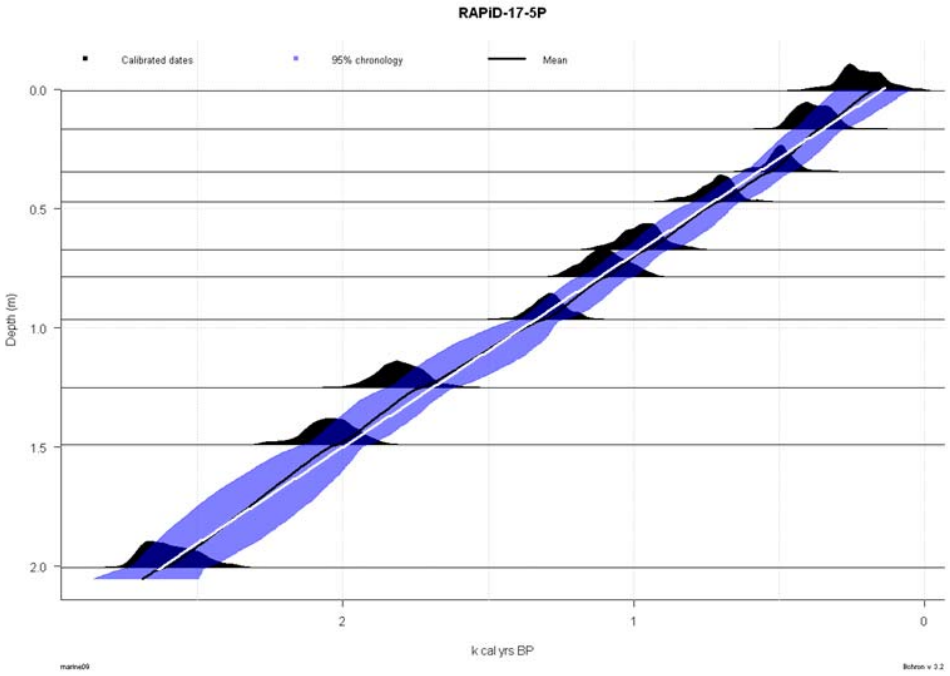

Figure S2. The Bayesian age-model obtained by Bchron (black) for the top 200cm of RAPiD-17-5P incorporating a local reservoir uncertainty (ΔR) of 50 years. The blue shaded area indicates the 95% probability based on the calibrated dates and calculated using the Bayesian statistical package, Bchron. The linear age model (in white) lies within the 95% probability envelope**.** The average difference between these age models during the study period is 22 years and the maximum is 46 years.

2. Supplementary notes

- **Pearson Correlation analysis**

Temperature from RAPiD-17-5P and TSI time-series were Gaussian interpolated at equal time-intervals 12.42 years with a 37.26 year window and a Pearson coefficient (Pt) was estimated employing the programme PearsonT[12]. A positive correlation of Pt=0.51 with a bootstrap error uncertainty of 0.31; 0.67 n=126 at >95% Confidence Level (CL) was obtained between the time-series with a time-lag of 12.42 years of the temperature with respect to the TSI forcing (Figure S3, Figure 2d Main text), which is within the combined dating uncertainty (Figure S2).

The 12.42 year lag present between the data and the TSI is where the Pt is greatest, however there are a couple of events at: (i) ~940 years AD and (ii) ~1010 years AD in the temperature that are slightly offset to the TSI and the (iii) 1250 years AD when temperature leads the TSI (Figure S3). None of the leads/lags exceed 40 years and are therefore within the dating uncertainties at these intervals.

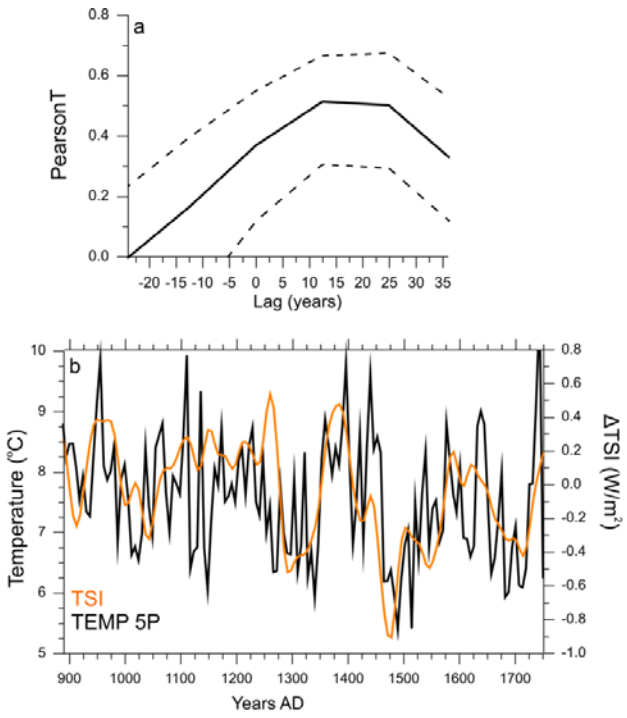

Figure S3. (a) Pearson coefficient at >95% CL of the correlation between the 12.42 year Gaussian interpolated RAPiD-17-5P temperature and ΔTSI[13] records at different time-lags. Dashed lines indicate the confidence interval. (b) Time series of the 12.42-year Gaussian interpolated RAPiD-17-5P temperature and ΔTSI with an applied 12.42 year lag.

- **Spectral analysis**

Power spectra were calculated using the multi-taper method[14] with seven data-tapers and spectral confidence levels located using the robust AR(1) modelling of median-smoothed spectra[15]. Cross-spectra used the algorithms of ref. 16. For the confidence levels of the power and coherency-spectra and the confidence intervals of the phase spectra we allowed for the effect of zero-padding[16]. Before analysis data were Gaussian interpolated to a common time interval of 6.21 years. The cross-spectra of the temperature reconstruction from RAPiD-17-5P and TSI exhibit high coherency at frequencies centred between 227-176 years at above 90% CL (Figure S4b,c) at a phase of 14-16 years (Figure S4d). The cross-spectral analysis reiterates the temperature-TSI correlation at periodicities similar to deVries solar cycles (200-210 years)[17].

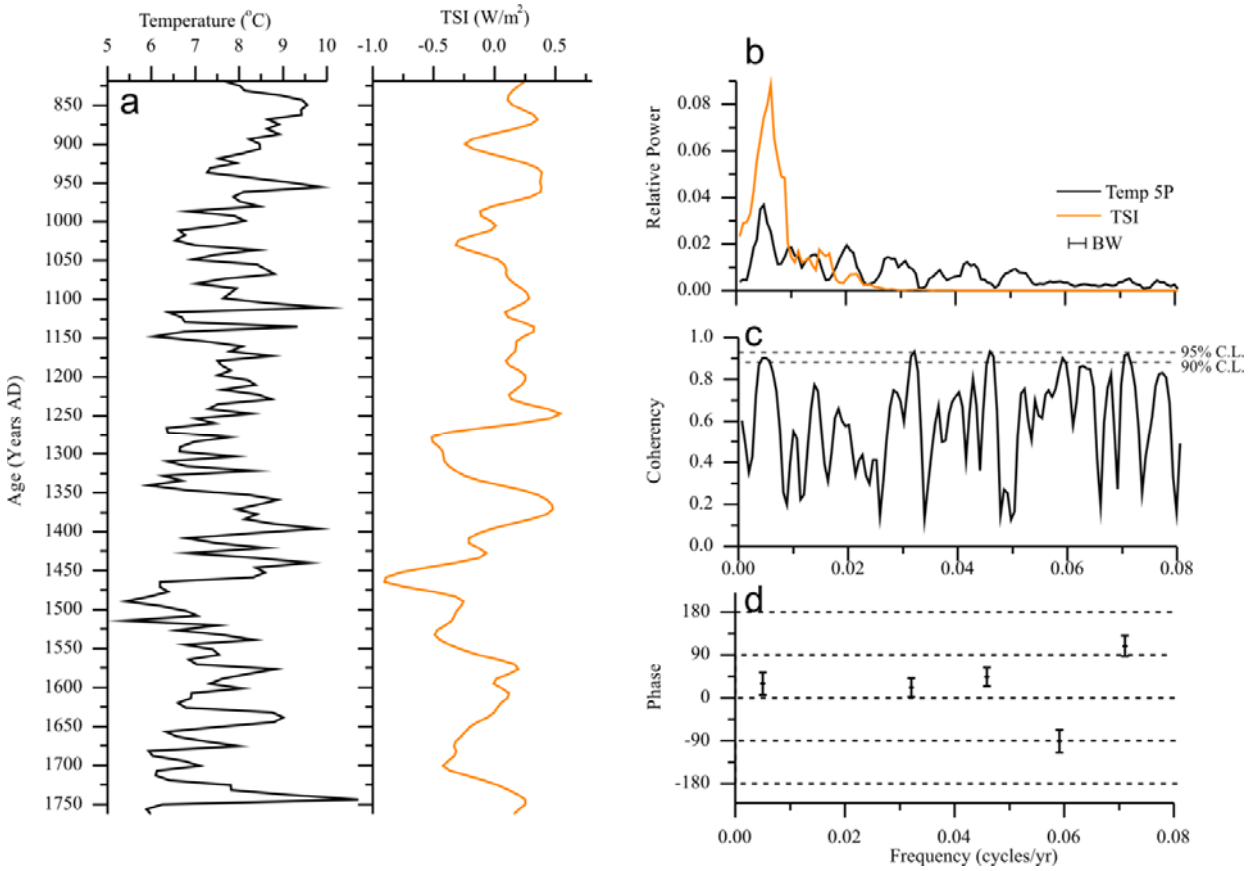

Figure S4. (a) Time-series of 6.21 year Gaussian smoothed temperature reconstruction from RAPiD-17-5P and TSI. (b) Single spectral analysis of RAPiD-17-5P temperature (black) and TSI (orange). (c) Coherence levels from the cross-spectral analysis of the temperature reconstruction from RAPiD-17-5P and TSI. Peaks are found at periodicities of 176-227 years AD (above 90% CL). Other peaks are also present at >90% C.L. at 30,16 and 14 years. However, we do not interpret these are they are only 5-2 times the spacing of the data. (d) Phase relationship between the frequency peaks of the two variables.

Wavelet analysis was also performed on the 6.21 year Gaussian interpolated zero-padded temperature record, using *Wavelet*[18]. Periodicities centred around 135-225 years were found to stand out over the background noise with significant power (>75%) at above 90 CL but are limited to 1200-1650 years AD (Figure S5a), albeit extending into the 'cone of influence' where possible edge effects may be increasingly important. To further support the linkage between solar irradiance and the NAC temperature, wavelet analysis was carried out on the 6.21 year Gaussian interpolated zero-padded ^{10}Be –based TSI reconstruction[13]. The results display a very similar temporal and spatial distribution of the power and particularly of the >90% CL envelope to that of the temperature reconstruction at periodicities centred at ~200 years between 1200-1650 years AD (Figure S5). Tentatively, the ~70-130-year cyclicities with less power (50-75%) found at 800-1200 years AD in the TSI may be similarly reflected in the temperature wavelet analysis.

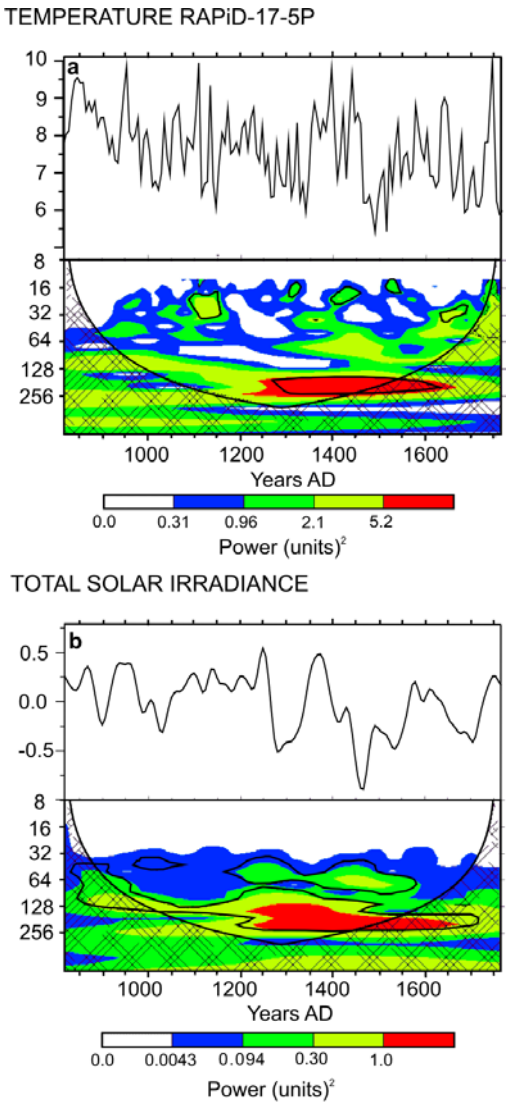

Figure S5. (a) Wavelet analysis on the 6.21- year Gaussian interpolated temperature record from RAPiD-17-5P using *Wavelet* [18]. (b) Wavelet analysis on 6.21-year Gaussian interpolated TSI from ref. 13. White, blue, green, yellow and red colours denote power above red-noise of 0, 15, 25, 50 and 75% respectively. The black outline indicates confidence level of 90% assuming a red-noise model.

- **Irminger Current proxy reconstructions from South Greenland (Eirik Drift)**

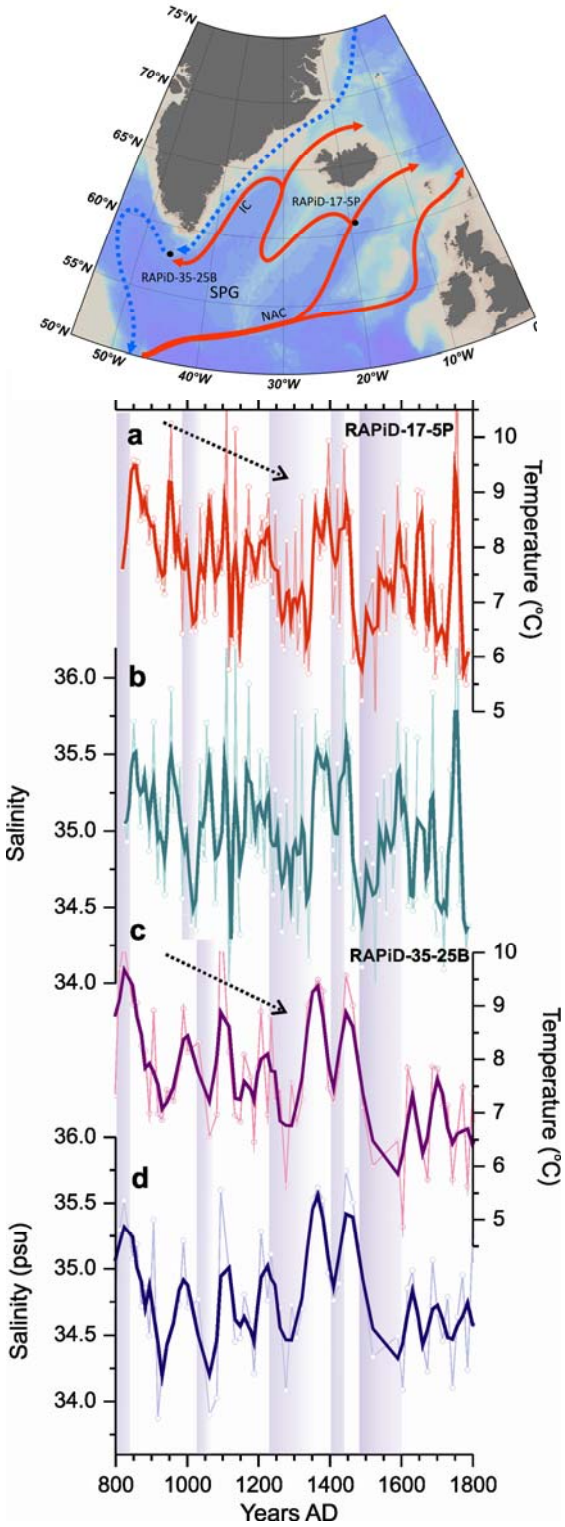

Figure S6 – Temperature and salinity reconstructions from RAPiD-17-5P (Iceland Basin) (a) and (b), and RAPiD-35-25B (SW Greenland) (d) and (e), respectively.

The core RAPiD-35-25B was recovered from the Eirik Drift (57° 30.47'N, 48° 43.40'W, 3486 m) and its core-chronology is based on 6 radiocarbon dates and present a linear sedimentation rate throughout the last 1200 years (available on request). In order to explore the properties of the Atlantic waters reaching the southern tip of Greenland via the Irminger Current[19] (inset map in Figure S6), we use the planktonic species *Globigerina bulloides*. The ecological preferences of *G. bulloides* for warm waters >7°C [20] is utilised in order to monitor the properties of the Irminger Current at the core site[19]. Paired Mg/Ca and $\delta^{18}O$ measurements on *G. bulloides* were made following the same methodology described above in the Supplementary Methods. The calibration Mg/Ca = 0.8 exp (0.081xT) from ref. 21 was used in order to calculate calcification temperatures.

Despite the lower temporal resolution of RAPiD-35-25B with respect to RAPiD-17-5P, we find broad similarities between these two records (Figure S6) which provide confidence that the two records are monitoring the same water mass. Additionally Figure S7 confirms this and shows that the temperature and salinity anomalies within the Atlantic waters are propagated westwards around the SPG as simulated in the model experiments.

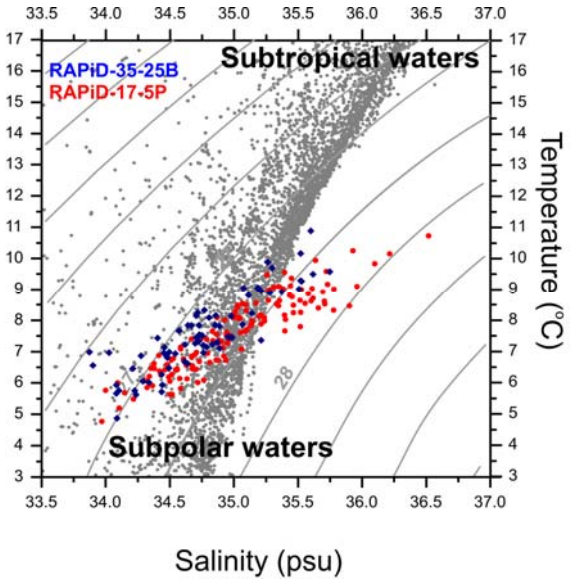

Figure S7. T/S plot of the temperature and salinity reconstructions from RAPiD-17-5P (red) and RAPiD-35-25B (blue). Grey points indicate T/S data points from the North Atlantic[22].

- **Comparison with other NAC records**

Results from RAPiD-17-5P compare quite well with other foraminiferal Mg/Ca records in the pathway of the NAC [23-25] or waters derived from this water mass[26], despite the lower temporal resolution in some of these (Figure S8).

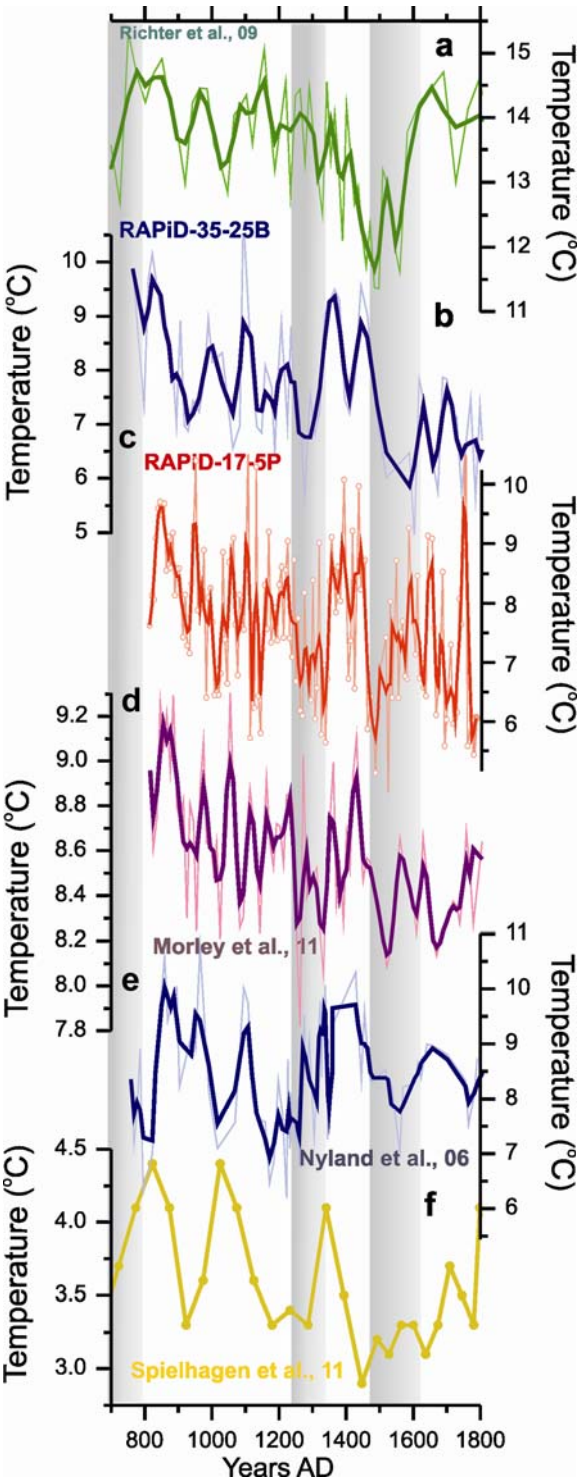

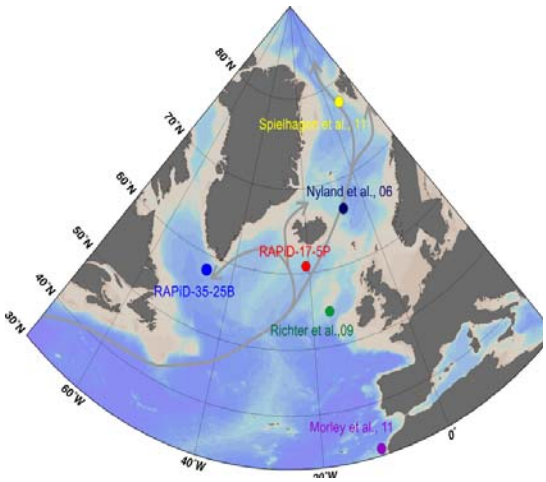

Figure S8. Foraminifera Mg/Ca-based temperature reconstructions from sites that are bathed by the Atlantic Inflow. (a) Richter et al. (2009), (b) RAPiD-35-25B presented in Chapter 3, (c) RAPiD-17-5P (this Chapter), (d) Morley et al. (2010), (e) Nyland et al. (2006), (f) Spielhagen et al. (2011). Grey shading shows some of the temperature minima. Map shows the colour-coded locations of the temperature reconstructions, grey arrows are schematic pathway of the Atlantic Inflow.

3. Supplementary Discussion:

- **Model analysis**

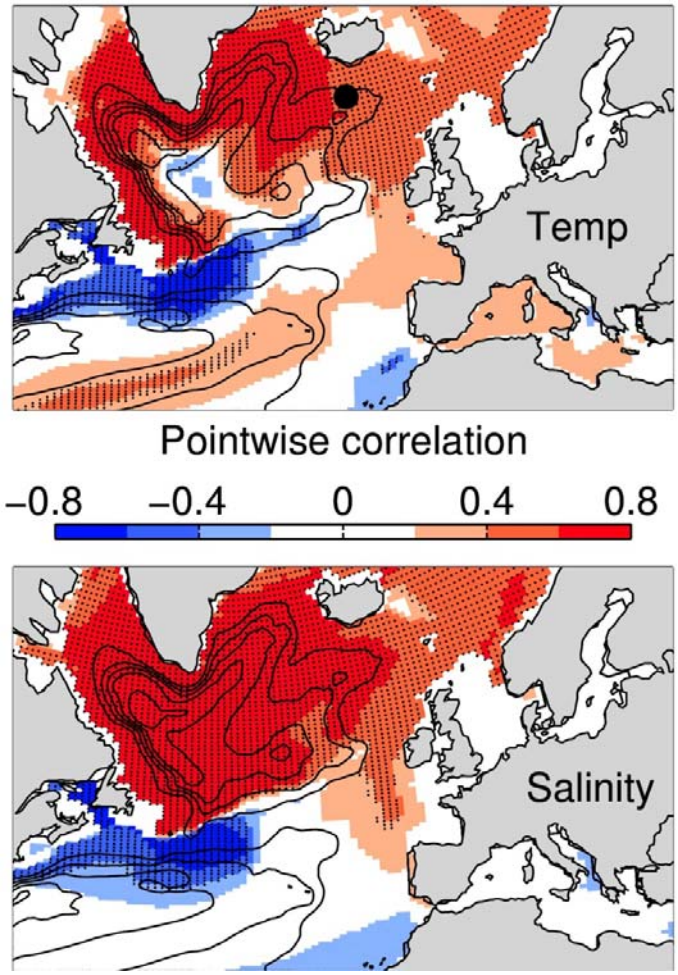

Figure S9. Pointwise correlation of 150-204 m averaged temperature and salinity with the SPG_AVE index. Statistically significant regions ($p<0.05$, $n=20$) are stippled. All data are low-pass filtered with a 50-year cut-off. High and statistically significant correlations are found at the core location and along the path of the boundary currents of the SPG, demonstrating the impact of heat and salt advection.

Salinity variations in the path of the Irminger Current are frequently interpreted as the result of the movement of the subpolar front[2,27]. However, advection of heat and salt also contribute considerably[28-31]. To illustrate the impact of the SPG circulation and associated advection on temperature and salinity at the relevant habitat depth of *G. inflata*, correlations are calculated between these two quantities (Figure S9). Both temperature and salinity are highly correlated with the strength of the SPG, here defined as the average of the barotropic stream function over the entire subpolar region, multiplied by -1 to obtain a positive index (SPG_AVE). High

correlation coefficients of up to 0.8 are seen for temperature throughout the boundary current system of the SPG, consistent with a dominant role of advection. The correlation of salinity with SPG_AVE results in high correlation coefficients in the entire SPG. For the boundary currents, this again is due to enhanced advection of saline subtropical waters from the NAC. In addition, the central SPG becomes more saline because of isopycnal outcropping that mixes more saline waters from deeper layers upward[32,33]. This is a common feature in climate models[33]. The same effect is seen in the correlation with temperature but since the deeper layers are colder, the correlation in the central SPG is negative in this case (Figure S9- Top panel). The NAC is shifted southward by a strong SPG, as seen in significantly colder and less saline water south of Newfoundland and corroborated by the proxy records from ref. 34.

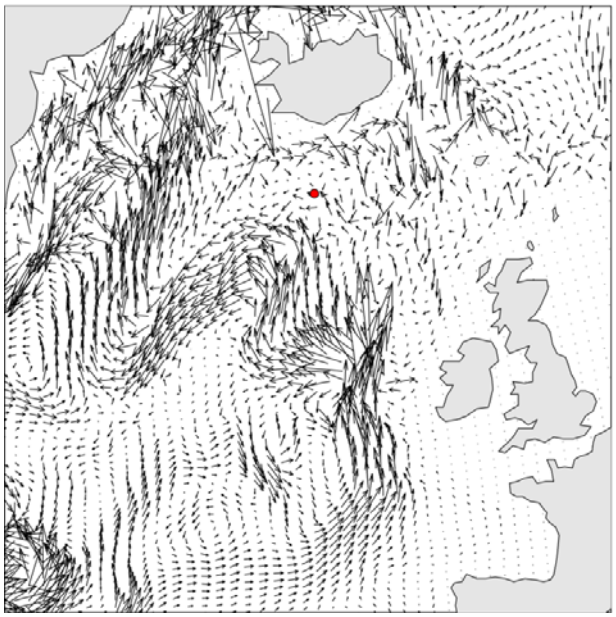

Figure S10. Regression of 150-204 m average velocity onto the normalized TSI (arbitrary units), low-pass filtered to exclude periods shorter than 50-years. With higher TSI the SPG circulation intensifies and more warm and saline waters of subtropical origin are advected to the core location (red dot) although the most pronounced circulation anomalies are further south.

As shown in the main text, the circulation of the SPG intensifies during periods of high TSI (Fig.3c in main text) but circulation anomalies directly at the core location south of Iceland are relatively small compared to the central SPG. This is partly explained by the definition of the stream function that, as a measure of integrated flow, shows the largest values not at the location of the currents themselves but in the mostly stagnant centre of the gyres. Analogously, the overturning stream function of the Atlantic Ocean is zero at the depth of southward flowing North Atlantic Deep Water. However, in Figure S10 the regression of velocities onto the normalized TSI index shows that changes in the flow are small at the core location indeed. The most pronounced anomalies are found further south. Several caveats apply to the comparison of model and reconstructed data at such fine detail, and while the sediment core is located at the core of the present-day NAC flow variations, present and past, do not necessarily be the largest there. Most importantly, this finding is consistent with the

interpretation that enhanced advection is the primary reason for temperature and salinity variations in the region.

Our interpretation of reconstructed variations in temperature and salinity is in disagreement with similar previous work on the same region[2]. These authors concluded that relatively fresh and cold water masses south of Iceland were the fingerprint of an anomalously strong SPG that shifted the subpolar front eastward, an idea originally proposed by ref. 27 from their analysis of the period 1960 to 2003. As pointed out above, our model results suggest that temperature and salinity variations are not the result of front movements but rather changes in advection and thus transport of heat and salt. Therefore, warm and saline conditions south of Iceland are the result of an anomalously strong SPG. The details of this mismatch have been addressed in a separate publication[33] and will be summarized here briefly.

The repeat analysis of the modelling data used in ref. 27 that led to the original interpretation of the salinity changes and variations in the SPG circulation[27] shows that the circulation anomaly that causes salinities to decrease south of Iceland is not representative of the entire SPG but rather a local recirculation (Fig. 1 of ref. 33). Furthermore, when the entire simulation period of Miami Isopycnic Coordinate Ocean Model (MICOM) 1950-2002 (model used by ref. 27) is taken into account (instead of 1960-2002), the circulation anomaly ceases to be the dominant mode of variability, but rather corresponds to the second empirical orthogonal function (EOF). The first EOF, representing a spin-up of the entire SPG, does not show a movement in the subpolar front south of Iceland or the corresponding salinity signal (Figure 2a of ref. 33). On the other hand, advection of salt does increase with a stronger SPG although the signal strength is too small and the simulation period too short to distinguish the impact of this effect in the regional model.

The analysis of salt transport in the SPG was extended to longer time-scales by using the Community Climate System Model version 4 (CCSM4) simulation of the last millennium[35]. Variability of the circulation as well as tracer advection compare favourably, lending confidence to the skill of CCSM4 because the regional model MICOM was designed to hind-cast the second part of the past century as realistically as possible. Since variations in the SPG circulation look similar in both models (MICOM and CCSM4) and include the entire SPG, we conclude that the circulation anomaly discussed by ref. 27, that inspired the conclusions of ref. 2, is probably specific to the second part of the last century and does not represent long-term dominant variations of the SPG as a whole.

- **Volcanic forcing sensitivity experiments**

In addition to the transient simulation of the last millennium, the sensitivity of the CCSM4 model to solar and volcanic forcing has been tested in a series of dedicated experiments. Starting from a preindustrial control simulation of 850 years duration, experiment SOL applies a reduction in TSI from the model preindustrial value of 1360.89 W/m^2 to 1360.00 W/m^2. This reduction approximates the decrease in solar radiation during solar minima in the forcing dataset that was used in the original transient simulation[36]. All other forcing components are invariable at their preindustrial default values, which is a reasonable approximation of the last millennium.

The effect of a series of volcanic eruptions is simulated in experiment VOLC, which is initiated identically as SOL, but transiently forced only by the series of volcanoes starting at year 1258 AD (Fig. 2 in main text). This series represents the period of strongest volcanic

activity of the last 1000 years, including the strongest single eruption recorded during this period. In the reconstruction as well as the transient simulation, this strong eruption at 1258 years AD coincides with the onset of the Wolf solar minimum, making it an ideal test case for the origin of the climatic signals that we reconstructed and modelled. However, it is also worth mentioning that CCSM4 has been found too sensitive to volcanic forcing[37].

Both sensitivity experiments were run for 50 years and compared to a continuation of the control experiment of the same length. Following the analysis in the main text, we compare key variables averaged over the years 11 to 50, to allow for some adjustment to the abrupt application of the anomalous forcing. The anomalous pattern of atmospheric sea surface pressure due to the reduced TSI is a high pressure anomaly centred over the British Isles (Figure S11- Top panel). This compares very well with the regression pattern found in the transient simulation. For anomalous volcanic forcing, a low pressure anomaly develops that is shifted southward (Figure S11- Bottom panel). Both shape and sign of this anomaly cannot explain the signal found in the transient simulation (Figure 4 in main text).

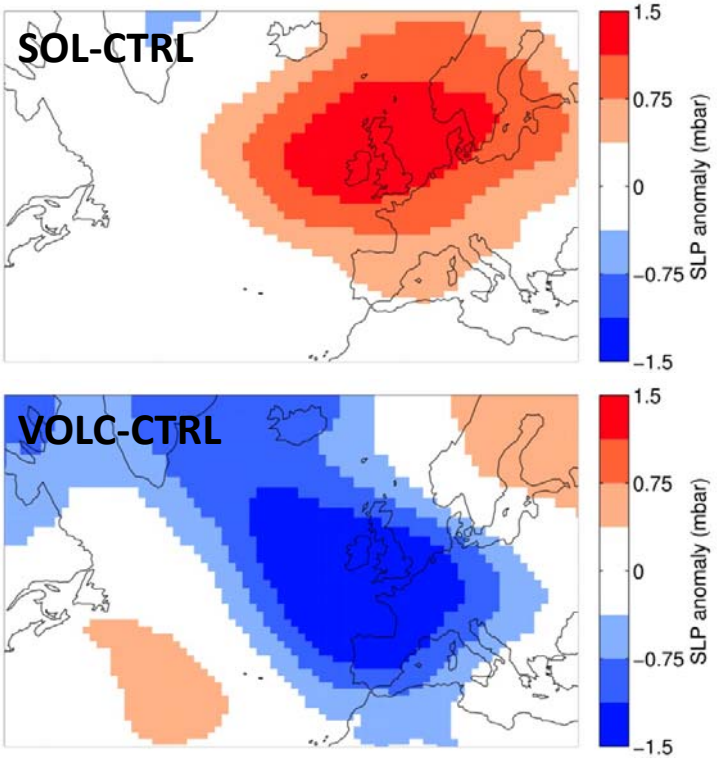

Figure S11. Anomaly of sea level pressure for experiment SOL (upper) and VOLC (lower). The anomalous pattern of SOL-CTRL agrees with findings in the transient simulation, while the response to volcanic forcing (VOLC-CTRL) is qualitatively different.

In agreement with the mechanism found in the transient simulation, the anomaly in SOL-CTRL results in a weakening of the SPG (Figure S12). The volcanic forcing experiment simulates a more complex change in the circulation with a weakening of the eastern part while the western SPG is stronger.

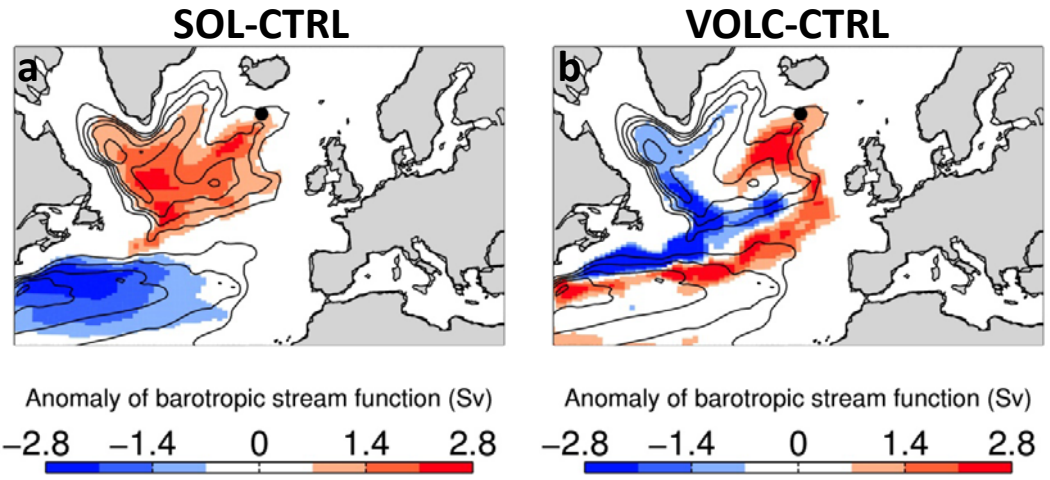

Figure S12. Difference of the depth-integrated stream function SOL-CTRL (a) and VOLC-CTRL (b). Only experiment SOL produces a circulation response in agreement with the transient simulation.

Lastly, we compare anomalies of temperature and salinity of the same depth range as in the transient simulation, the habitat depth of *G. inflata* (Figure S13). Here, the comparison with the corresponding correlations in the transient simulation (Figure 3 in main text) must remain more qualitative because correlations cannot be calculated for the sensitivity experiments. Both, experiment SOL and VOLC, simulate a cooling at the location of RAPiD-17-5P. However, only the solar forcing case explains decreasing temperatures along the path of the Irminger Current and the Labrador Sea boundary current system, as found in the transient simulation. Note also, that this is a requirement for in-phase cooling both in the Iceland Sea (RAPiD-17-5P) and on Eirik Drift (RAPiD-35-25B, Figure S6). Analysis of the salinity anomalies reinforces the conclusion that SOL and VOLC simulate fundamentally different dynamic changes. While the salinity anomalies in SOL support findings from the transient simulation, VOLC simulates strong anomalies on a larger spatial scale (Figure S13).

We therefore conclude that changes in solar forcing consistently explain the key changes described in the transient simulation while anomalous volcanic forcing yields a qualitatively different dynamic response of the atmosphere-ocean system in our region of study. For the model-data comparison, we note that both anomalous forcing components qualitatively explain a cooling of the Iceland Sea, but only the solar forcing causes a simultaneous cooling at Eirik Drift south of Greenland that was found in a second reconstruction.

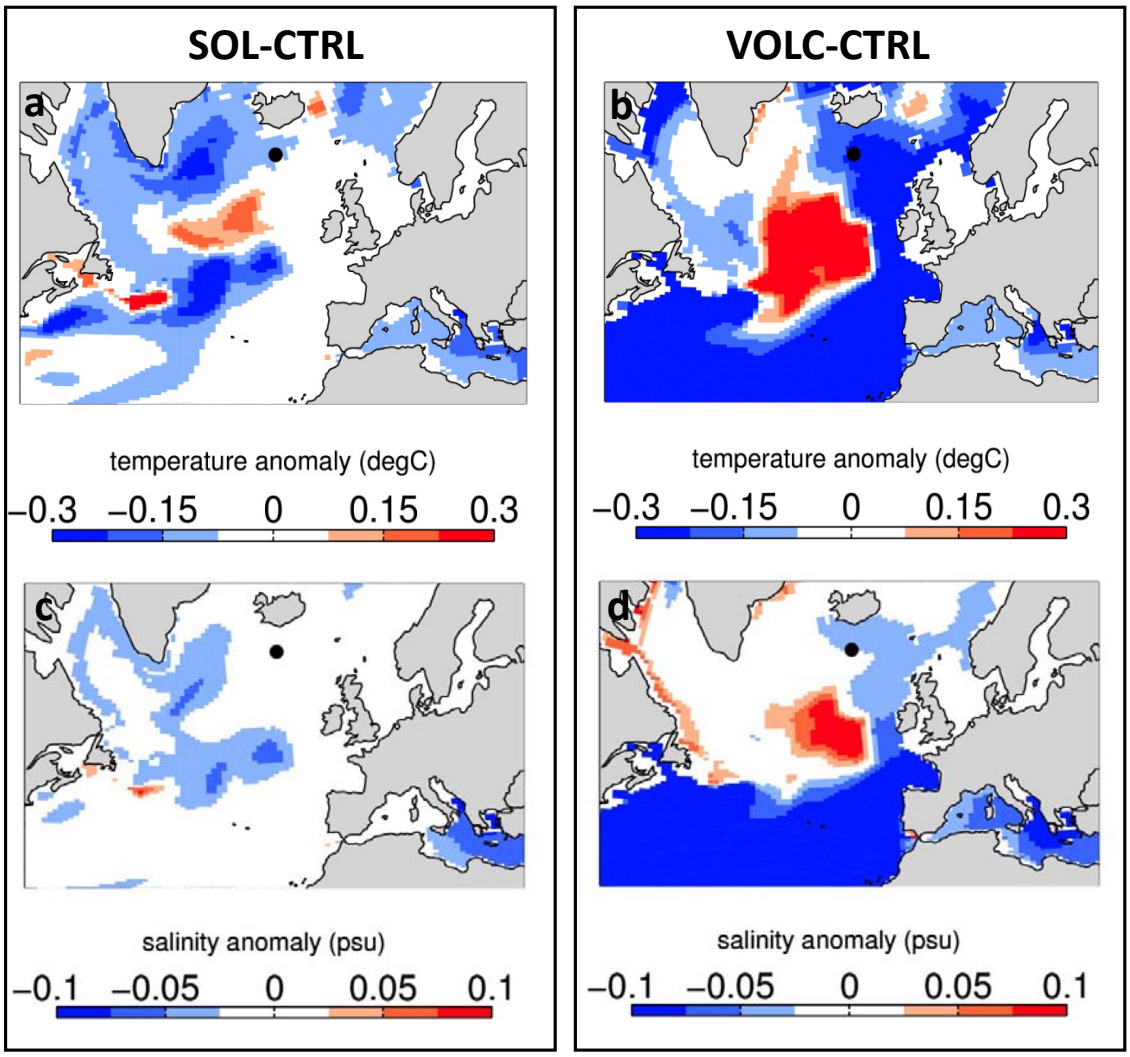

Figure S13. Differences of temperature and salinity averaged over a depth from 150-204m, for SOL-CTRL (left column-(a,c)) and VOLC-CTRL (right column (b,d)). In-phase cooling in the Iceland Basin and on Eirik Drift is simulated for solar (a) but not volcanic forcing (b). Decreasing salinities are found for SOL-CTRL in the subpolar gyre (c), as expected from the analysis of the transient simulation (Figure 3). However, salinity changes in experiment VOLC-CTRL (d) suggest a fundamentally different dynamic response in the ocean circulation.

- **Regression of winter SLP on TSI**

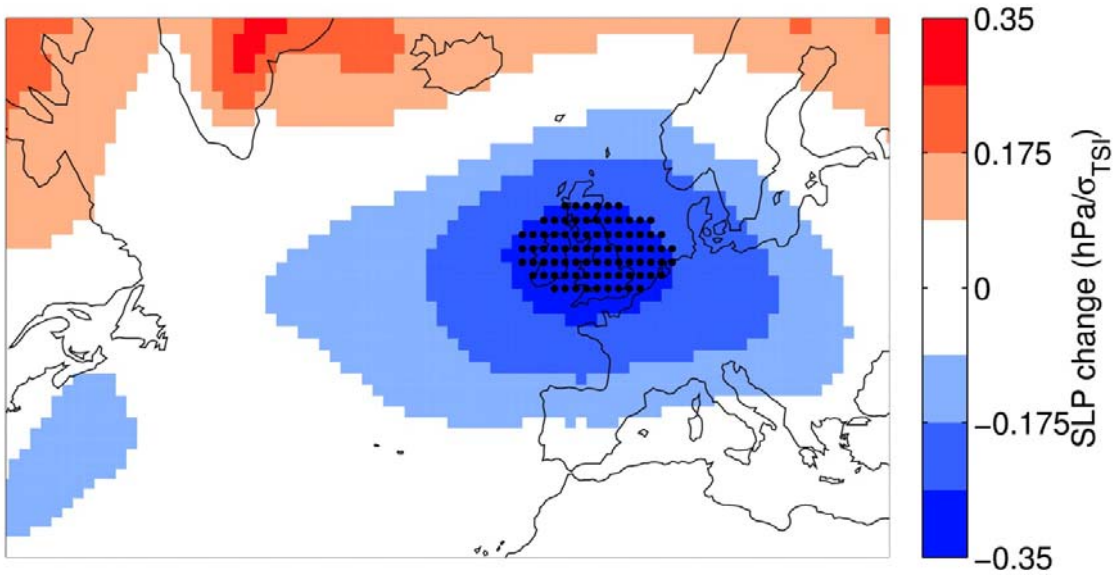

Figure S14. SLP analysis of CCSM4 reveals an anomalous high pressure system during low TSI over the British Isles and the eastern North Atlantic indicative of increased winter blocking. Time-series have been filtered with a 50 year low-pass filter. Areas above 95% confidence threshold are marked with dots.

References:

1 Barker, S., Greaves, M. & Elderfield, H. A study of cleaning procedures used for foraminiferal Mg/Ca paleothermometry. *Geochemistry Geophysics Geosystems* 4, 8407 (2003).

2 Thornalley, D. J. R., Elderfield, H. & McCave, I. N. Holocene oscillations in temperature and salinity of the surface subpolar North Atlantic. *Nature* 457, 711-714 (2009).

3 Kim, S.-T. & O'Neil, J. R. Equilibrium and nonequilibrium oxygen isotope effects in synthetic carbonates. *Geochimica et Cosmochimica Acta* 61, 3461-3475 (1997).

4 LeGrande, A. N. & Schmidt, G. A. Global gridded data set of the oxygen isotopic composition in seawater. *Geophysical Research Letters* 33 (2006).

5 Schmidt, G. A. Error Analysis of Paleosalinity Calculations. *Paleoceanography* 14, 422-429 (1999).

6 Reimer *et al. INTCAL09 and MARINE09 Radiocarbon age calibration curves, 0-50,000 years Cal BP*. Vol. 51 (University of Arizona, 2009).

7 Stuiver, M., Reimer, P. J. & Braziunas, T. F. *High-precision radiocarbon age calibration for terrestrial and marine samples* (1998).

8 Sicre, M. A. *et al.* Sea surface temperature variability in the subpolar Atlantic over the last two millennia. *Paleoceanography* 26 (2011).

9 McCave, I. N. CD159 Cruise Report. (2004).

10 Haslett, J. & Parnell, A. A simple monotone process with application to radiocarbon-dated depth chronologies. *Journal of the Royal Statistical Society: Series C (Applied Statistics)* 57 (2008).

11 Parnell, A. C., Haslett, J., Allen, J. R. M., Buck, C. E. & Huntley, B. A flexible approach to assessing synchroneity of past events using Bayesian reconstructions of sedimentation history. *Quaternary Science Reviews* 27, 1872-1885 (2008).

12 Mudelsee, M. Estimating Pearson's correlation coefficient with bootstrap confidence interval from serially dependent time series. *Mathematical Geology* 35, 651-665 (2003).

13 Steinhilber, F., Beer, J. & Fröhlich, C. Total solar irradiance during the Holocene. *Geophysical Research Letters* 36 (2009).

14 Pardoiguzquiza, E., Chicaolmo, M. & Rodrigueztovar, F. J. CYSTRATI - A computer program for spectral-analysis of stratigraphic successions *Computers & Geosciences* 20 (1994).

15 Mann, M. E. & Lees, J. M. Robust estimation of background noise and signal detection in climatic time series. *Climatic Change* 33, 409-445 (1996).

16 Bloomfield, P. *Fourier analysis of time series: An introduction*. (John Wiley & Sons, 1976).

17 Braun, H. *et al.* Possible solar origin of the 1,470-year glacial climate cycle demonstrated in a coupled model. *Nature* 438, 208-211 (2005).

18 Torrence, C. & G. P. Compo. A Practical Guide to Wavelet Analysis. *Bulletin American Metereological Society* 79, 61-78 (1998).

19 Holliday, N. P., Bacon, S., Allen, J. & McDonagh, E. L. Circulation and transport in the western boundary currents at Cape Farewell, Greenland. *Journal of Physical Oceanography* 39, 1854-1870 (2009).

20 Hilbrecht, H. (ed Neue Folge Mitteilungen aus dem Geologischen Institut der Eidgen. Technischen Hochschule und der Universität Zürich) (Zürich, 1996).

21 Elderfield, H. & Ganssen, G. Past temperature and $\delta^{18}O$ of surface ocean waters inferred from foraminiferal Mg/Ca ratios. *Nature* 405, 442-445 (2000).

22 Key, R. M. *et al.* A global ocean carbon climatology: Results from Global Data Analysis Project (GLODAP). *Global Biogeochemical Cycles* 18, GB4031 (2004).
23 Nyland, B. F., Jansen, E., Elderfield, H. & Andersson, C. Neogloboquadrina pachyderma (dex. and sin.) Mg/Ca and δ18O records from the Norwegian Sea. *Geochemistry, Geophysics, Geosystems* 7 (2006).
24 Richter, T. O., Peeters, F. J. C. & van Weering, T. C. E. Late Holocene (0-2.4 ka BP) surface water temperature and salinity variability, Feni Drift, NE Atlantic Ocean. *Quaternary Science Reviews* 28, 1941-1955 (2009).
25 Spielhagen, R. F. *et al.* Enhanced Modern Heat Transfer to the Arctic by Warm Atlantic Water. *Science* 331, 450-453 (2011).
26 Morley, A. *et al.* Solar modulation of North Atlantic central Water formation at multidecadal timescales during the late Holocene. *Earth and Planetary Science Letters* 308, 161-171 (2011).
27 Hátún, H., Sandø, A. B., Drange, H., Hansen, B. & Valdimarsson, H. Influence of the Atlantic Subpolar Gyre on the Thermohaline Circulation. *Science* 309, 1841-1844 (2005).
28 Desprès, A., Reverdin, G. & d'Ovidio, F. Mechanisms and spatial variability of meso scale frontogenesis in the northwestern subpolar gyre. *Ocean Modelling* 39, 97-113 (2011).
29 Häkkinen, S., Rhines, P. B. & Worthen, D. L. Warm and saline events embedded in the meridional circulation of the northern North Atlantic. *J. Geophys. Res.* 116 (2011).
30 Born, A., Nisancioglu, K. H. & Braconnot, P. Sea ice induced changes in ocean circulation during the Eemian. *Climate Dynamics* 35, 1361-1371 (2010).
31 de Boisséson, E., Thierry, V., Mercier, H., Caniaux, G. & Desbruyères, D. Origin, formation and variability of the Subpolar Mode Water located over the Reykjanes Ridge. *Journal of Geophysical Research: Oceans* 117 (2012).
32 Häkkinen, S. & Rhines, P. B. Decline of Subpolar North Atlantic Circulation During the 1990s. *Science* 304, 555-559 (2004).
33 Born, A. T. F. S., A.B. Sando. Coupling of eastern and western subpolar NorthAtlantic: salt transport in the Irminger Current. *Ocean Science Discussions* 10, 555-579 (2013).
34 Keigwin, L. D. & Pickart, R. S. Slope water current over the Laurentian Fan on interannual to millennial time scares. *Science* 286, 520-523 (1999).
35 Landrum, L. *et al.* Last Millennium Climate and Its Variability in CCSM4. *Journal of Climate* (2012).
36 Vieira, L. E. A., Solanki, S. K., Krivova, N. A. & Usoskin, I. Evolution of the solar irradiance during the Holocene. *Astronomy and Astrophysics* 531 (2011).
37 Gent, P. R. *et al.* The Community Climate System Model Version 4. *Journal of Climate* 24 (2011).